Comparison of IASI water vapor retrieval with H_2O-Raman lidar in the frame of the Mediterranean HyMeX and ChArMEx programs

Patrick Chazette, Fabien Marnas, Julien Totems and Xiaoxia Shang

Laboratoire des Sciences du Climat et de l'Environnement (LSCE), UMR8212, Laboratoire mixte CEA-CNRS-UVSQ, CEA Saclay, 91191 Gif-sur-Yvette, France.

Abstract.

The Infrared Atmospheric Sounding Interferometer (IASI) is a spaceborne passive sensor of new generation mainly dedicated to meteorological applications. Operational Level-2 products are available via the European Organisation for the Exploitation of Meteorological Satellites (EUMETSAT) since several years. In particular, vertical profiles of water vapor measurements are retrieved from infrared radiances at the global scale. Nevertheless, the robustness of such products has to be checked because only few validations have been reported. For this purpose, the field experiments that were held during the HyMeX and ChArMEx international programs are a very good opportunity. A H_2O-Raman lidar was deployed on the Balearic Island of Menorca and operated continuously during ~6 and ~3 weeks during fall 2012 (Hydrological cycle in the Mediterranean eXperiment -HyMeX-) and summer 2013 (Chemistry-Aerosol Mediterranean Experiment -ChArMEx-), respectively. It measured simultaneously the water vapor mixing ratio and aerosol optical properties. This article does not aim to describe the IASI operational H_2O inversion algorithm, but to compare the vertical profiles derived from IASI onboard MetOp-A and the ground-based lidar measurements to assess the reliability of the IASI operational product for the water vapor retrieval in both the lower and middle troposphere. The links between water vapor contents and both the aerosol vertical profiles and the air mass origins are also studied. About 30

simultaneous observations, performed during nighttime in cloud free conditions, have been considered. For altitudes ranging from 2 to 7 km, root mean square errors (correlation) of ~0.5 g/kg (~0.77) and ~1.1 g/kg (~0.72) are derived between the operational IASI product and the available lidar profiles during HyMeX and ChArMEx, respectively. The values of both root mean square error and correlation are meaningful and show that the operational Level-2 product of the IASI-derived vertical water vapor mixing ratio can be considered for meteorological and climatic applications, at least in the frame of field campaigns.

1 Introduction

Satellite observations are powerful tools for meteorological forecast. Their assimilation in models lead to an improvement on weather forecasts (e.g. *Collard and McNally*, 2009; *Bormann et al*., 2010). Among the main components of the atmospheric state, water vapor is an essential element, which plays a key role in frontogenesis, convection (e.g. *Held and Soden*, 2000), cloud formation and aerosol hydration (e.g. *Larson and Taylor*, 1983; *Rood et al*., 1987; *Randriamiarisoa et al*., 2006). In this way, it influences significantly the Earth climate and the atmospheric chemistry (e.g. IPCC, 2014). It is also an energy reservoir that exchanges with both the atmosphere and the surface through condensation and evaporation processes via the latent heat flux. Hence, for reliable weather forecasts, the vertical profile of the water vapor has to be precisely assessed.

During several decades, passive radiometers, such as those implemented onboard of the Televison InfraRed Operational Satellite (TIROS) from the National Oceanographic and Atmospheric Administration (NOAA), have allowed to retrieve temperature and moisture profiles with a vertical resolution of about 3 to 5 km in the troposphere, as defined by the instrumental weighting functions (e.g. *Susskind et al*., 1984; *Chedin et al*., 1985). A new generation of instruments has been launched on polar platforms satellites, such as

Interferometric Monitor for Greenhouse gases (IMG, e.g. Ogawa et al., 1994; Clerbaux et al., 1998), Tropospheric Emission Spectrometer (TES, e.g. *Shephard et al*., 2008; *Worden et al*., 2012), the Advanced Infrared Sounder (AIRS, *Chahine et al*., 1990; *Aumann and Miller*, 1995), and the Infrared Atmospheric Sounding Interferometer (IASI, e.g. *Clerbaux et al*., 2009; *Hilton et al*., 2012). Thanks to a larger number of spectral channels and an enhanced spectral resolution, these instruments lead to improved vertical resolutions down to 1 km and higher precision of both the atmospheric temperature and water vapor content retrieval.

We will focus our study on the reliability of the water vapor mixing ratio (WVMR) vertical profiles retrieved from the IASI spectrometer, which has been launched onboard the polar orbiting meteorological satellites MetOp (Meteorological Operational), which forms the space segment of the overall EUMETSAT Polar System (EPS).

Main mission of IASI is the operational meteorology (e.g. *Zhou et al*., 2009), although air-composition and climate applications are also well covered by the instrument as also discussed before launch (e.g. *Chazette et al*., 1998; *Clerbaux et al*., 1998) and now demonstrated (e.g. *Crevoisier et al*., 2013a; *Griffin et al*., 2013; *Grieco et al*., 2013). Hereafter we will only discuss the comparison between IASI-derived WVMR and the simultaneous measurements performed by a H_2O-Raman lidar deployed on the Balearic Island of Menorca in the frame of the Hydrological cycle in the Mediterranean eXperiment (HyMeX, http://www.hymex.org/, *Chazette et al*., 2013) and Chemistry-Aerosol Mediterranean Experiment (ChArMEx, http://www.mistrals-home.org).

For our concern, the IASI-derived WVMR operational Level-2 products have been available via the European Organisation for the Exploitation of Meteorological Satellites (EUMETSAT) for several years. In particular, vertical profiles of WVMR measurements are retrieved from infrared radiances at the global scale (e.g. *Carissimo et al*., 2005; *Schlüssel et*

74 *al*., 2005; *Schneider and Hase*, 2011). The robustness of such products has to be checked, and
75 the field experiments that were held during the HyMeX and ChArMEx international programs
76 are a very good opportunity for that purpose. Few validation exercises have been conducted
77 on the WVMR operational product. The main reason seems that for meteorological
78 forecasting, the radiances are directly assimilated in the models (e.g. *Hilton et al*., 2009;
79 *Hilton et al*., 2012; *Heilliette*, 2013; *Matricardi and McNally*, 2013; *Xu et al*., 2013).
80 Nevertheless, the WVMR Level-2 product could have a great interest in order to help field
81 experiment analyses. Moreover, few validations are available in the scientific literature.
82 *Pougatchev et al*. (2009) used rawindsounding measurements to assess the error covariance
83 matrix needed for the inversion algorithm. *Masiello et al*., (2013) argue that lidar
84 measurements are excellent candidates for the validation of spaceborne sensors. They used
85 different measurement techniques during the Convective and Orographically-induced
86 Precipitation Study (COPS) campaign, and the comparisons were performed with a limited
87 number of lidar profiles (6) during the same season. Such validations are very delicate
88 because performing atmospheric measurements of WVMR with the required accuracy for
89 satellite retrieval validation is a challenging issue due to the high spatio-temporal variability
90 of atmospheric water vapor. The spatiotemporal coincidence between the ground-based and
91 the spaceborne measurements has to be guaranteed to avoid important sampling errors.

92 In the following section, the Raman lidar system used for IASI WVMR comparisons and its
93 technical specifications will be presented as well as the experimental sites used to conduct the
94 validation during the Mediterranean project. The IASI derived WVMR product specifications
95 will also be introduced. The third section will present the experimental comparisons. The
96 statistical tools used to evaluate the WVMR products will be introduced and the experimental
97 results obtained will be presented. Then, the influence of both the air mass origin and their

aerosol content in the results will be discussed. Finally, the main results will be recalled in the conclusion.

2 Observations

The comparison between the WVMR ground-based lidar measurements and the IASI operational products took place in the frame of both HyMeX and ChArMEx Special Observation Periods during September-October 2012 and June-July 2013, respectively, on the Balearic island of Menorca. During HyMeX/IODA-MED (Innovative Observing and Data Assimilation systems for the MEDiterranean Weather), the Water vapour and Aerosol lidar (WALI) was located close to La Ciutadella (Western part of the island, 39°60'00" N and 3°50'20"E), while during ChArMEx it was deployed close to Mahon (Eastern part of the island, 39°53’12” N and 4°15’31” E). Hence, the WVMR vertical profiles derived from the IASI spaceborne spectrometer (Ether CNES/CNRS-INSU Ether web site http://www.pole-ether.fr) have been compared to the ones measured by WALI during nighttime for field experiment durations of 6 and 3 weeks for HyMeX and ChArMEx, respectively. The use of the Raman technique limits the range of daytime measurements (< 1 km), which are consequently not relevant for a validation purpose in the lower and middle troposphere.

2.1 The WALI Raman lidar

The WALI instrument uses an emitting wavelength of 354.7 nm and is designed to fulfill eye-safe conditions (Table 1). The instrument, its calibration and the associated errors are documented in *Chazette et al*. (2013) and will not be detailed here. During all the experiment the acquisition was performed for mean profiles of 1000 laser shots leading to a temporal sampling close to 1 minute. The UV pulse energy is ~60 mJ and the pulse repetition frequency is 20 Hz. It is equipped with four detection channels: an aerosol board including co-polarized and cross polarized channels with respect to the laser emission, a channel

dedicated to the detection of the water vapor Raman signal at 407.5 nm and a fourth channel dedicated to the recording of the atmospheric nitrogen Raman signal at 386.6 nm.

The design of the WALI system leads to very good capabilities in terms of low altitude overlap and WVMR retrieval during nighttime. The absolute deviation from rawindsoundings is less than 0.5 g/kg (*Chazette et al*., 2013). The error on the WVMR reaches 11% in the marine boundary layer and decreases to 7% below 5 km range for a temporal averaging of 20 minutes and a vertical resolution of 15 m. Precision can deteriorate very quickly thereafter due to the decreasing Signal to Noise Ratio (SNR) with altitude. It is also worse during daytime, but measurements can be performed with the same uncertainty for altitude ranges below 1 km using a temporal averaging over ~1 hour. For the inter-comparisons presented in this paper, the chosen averaging time is 30 minutes, centered on the time value of the IASI profile to be compared, and the altitude range is from 0.3 to 7 km above the mean sea level (amsl). The original vertical and temporal resolutions are 15 m and 1 minute, respectively. The lidar profiles were smoothed for the comparison so that the vertical resolution used for this study is ~41 m.

2.2 The MetOp /IASI satellite data

MetOp (Meteorological Operational) consists of a series of three polar heliosynchronous orbiting satellites, to be flown successively for more than 14 years, from 2006. This series forms the space segment of the overall EUMETSAT Polar System (EPS). EPS is the European contribution to the Initial Joint Polar System agreement (IJPS), an agreement between EUMETSAT and NOAA. MetOp flies in a Low Earth orbit at an altitude of 817 km corresponding to local 'morning', while the US is responsible for 'afternoon' coverage (*Klaes et al*., 2007). MetOp-A (launched on 19 October 2006) and MetOp-B (launched on 17 September 2012) provide detailed observations of the global atmosphere, oceans and

146 continents. MetOp-C is due to be launched in 2017. The series provides data for both
147 operational meteorology and climate studies. A combination of passive remote sensing
148 instruments offers the capability to observe the Earth by day and night, as well as under
149 cloudy conditions. The most innovative and one of the key instruments on MetOp is the
150 Michelson interferometer IASI. Three IASI instruments were developed for MetOp by CNES
151 (Centre National d'Etudes Spatiales) in cooperation with EUMETSAT. They are built to
152 provide temperature and moisture measurements with unprecedented accuracy and resolution,
153 and additionally to provide information for the monitoring of atmospheric trace gases.

154 The bandwidth of IASI is divided into 8461 spectral channels between 645 and 2760 $cm^{-1}$with
155 a mean spectral resolution of 0.5 cm^{-1} after apodization. IASI scans across-track in 30
156 successive elementary fields of view (EFOV), each composed of 4 instantaneous fields of
157 view (IFOV) of 0.8225° leading to a footprint of 12 km diameter at sub-satellite point. The
158 footprint dimension increases from 20 to 39 km along-track directions to the swath edge,
159 respectively (*Cayla*, 1993). The swath width on the ground is approximately 2200 km, which
160 provides global Earth coverage twice per day.

161 Operational products from EPS/MetOp are generated in the EPS Core Ground Segment. The
162 IASI Level-2 processing development targeted the generation of temperature and humidity
163 profile information, the associated surface information and the retrieval of some trace gas
164 species: CO, O_3, CH_4, N_2O and CO_2. The vertical temperature and water-vapor profiles are
165 currently distributed on a 90-level grid extending between 0.005 and 1050 hPa (*August et al*.,
166 2012). Note that the operational product uses a statistical approach to retrieve the geophysical
167 parameters. Other approaches use a physical scheme and give access to a better vertical
168 resolution (e.g. *Amato et al*., 2009; *Masiello et al*., 2013). Nevertheless, the goal of this paper

is to provide quantitative elements of validation for the operational product using the statistical approach.

Both the temperature and moisture of the troposphere and lower stratosphere are derived under cloud-free conditions with a vertical resolution of 1-2 km in the lower troposphere; a horizontal resolution of 25 km, and an accuracy of 1 K and 10%, respectively. The number of independent pieces of information which are determined in the moisture profiles is in the order of 10. The sensitivity to the lower troposphere is lower and leads to larger error beneath 3 km, although ~80% of moisture is contained in this layer. For the WVMR retrieval, the IASI weighting functions are generally maximum above 700 hPa.

For the comparison presented hereafter, we considered the 12 closest IASI pixels from the lidar ground-based station. The mean values and the associated standard deviations are then calculated if the number of relevant IASI-derived WVMR profiles are at least equal to 6.

3 Comparison between the IASI and WALI water vapor products

Here we assess the representativeness of IASI in terms of atmospheric moisture content considering both vertical profiles and integrated values to evaluate the potentiality of these products to be used for meteorological studies purposes. The relevant IASI coincidences are established before a comparison with the Raman lidar WALI separately for the two time periods of field experiments.

3.1 Coincidences

Figure 1 gives the temporal evolution of the WVMR vertical profiles above Menorca during the two time periods on which field experiments were conducted. The water vapor contents are highly variable and highlight contrasted atmospheric situations, which are of interest for comparison to IASI-derived WVMR. On the same figure are given the satellite overpass times for which comparisons are relevant. We have identified 30 coincidences in cloud-free

conditions with available IASI profiles, during September-October 2012 and June-July 2013. Note that the presence of high aerosol content is also classified as a cloudy condition. For each time period, the coincidences are identified by their number in a chronological way hereafter called coincidence number (CN). All the coincidences are reported in Table 2 and Table 3 for the time periods of HyMeX and ChArMEx, respectively (15 CN each). The distance between the central pixel of IASI and the lidar ground-based station (*D*), and the number of relevant IASI pixels (*N*) are also indicated.

3.2 WVMR vertical profiles

The WVMR vertical profiles for the whole retained atmospheric situations are shown in Figure 2 and Figure 3 for HyMeX and ChArMEx, respectively. The coincident WVMR simulated from the European Centre for Medium-range Weather Forecasts (ECMWF) operational analysis are also plotted on the figures. The 9 closest model grids from the ground-based lidar station are considered to compute both the mean and the standard deviation vertical profiles. The meteorological fields have been provided by ECMWF and have been obtained from the ESPRI/IPSL data server for a horizontal resolution of 0.5°.

The statistical indicators used to evaluate the relevance of the IASI-derived WVMR (r_{iasi}) with respect to lidar observations (r_{lidar}) are the Root Mean Square Error (RMSE) and the (Pearson) correlation (COR). They are often used to evaluate model performances as in *Boylan and Russell* (2006) and can be written as

$$RMSE = \sqrt{\frac{1}{N_t}\sum_{i=1}^{N_t}(r_{iasi} - r_{lidar})^2} \quad (1)$$

$$COR = \frac{\sum_{i=1}^{N_t}(r_{lidar}-\overline{r_{lidar}})(r_{iasi}-\overline{r_{iasi}})}{\sqrt{\sum_{i=1}^{N_t}(r_{lidar}-\overline{r_{lidar}})^2 \sum_{i=1}^{N_t}(r_{iasi}-\overline{r_{iasi}})^2}} \quad (2)$$

where N_t is the total number of coincidences and the overbar terms are averages. The vertical values for both r_{IASI} and r_{lidar} are used at the IASI-L2 pressure level gird.

Figure 4 gives the vertical profiles of both RMSE and COR for the two time periods. The statistical indicators have been computed between WALI and IASI, and WALI and ECMWF data.

During the first time period (fall time), the lidar and modelled profiles are in better agreement with a mean RMSE and COR of 0.42 g/kg and 77% (between 0.5 and 7 km), respectively, whereas between the lidar and IASI vertical profiles these values reach ~0.6 g/kg and 70%, respectively. The shapes of RMSE and COR against altitude are however very similar. It is not surprising because ECMWF analyses are made by assimilating the IASI radiances (e.g. *Hilton et al*., 2012) in addition to the rawinsounding performed in Palma de Mallorca (100 km Southwest of Menorca). In the planetary boundary layer (PBL) more discrepancy could be encountered due to local effects.

An opposite behavior happens in terms of RMSE for the second time period (summer time) where the IASI-derived WVMR (*RMSE* = 1.64 g/kg) is better than that of the model (*RMSE* = 2.04 g/kg) when compared to the Raman lidar. It is mainly true below 2 km. Nevertheless, the correlation is better between the lidar and the ECMWF analyses (0.82) than between the lidar and IASI (0.59).

In the free troposphere, where the IASI weighted functions mostly have their maxima, the agreement is better according to the two indicators that are the COR and RMSE indicators. This agreement is higher for the HyMeX time period and might be due to a lesser influence of the aerosol layers. For this period *RMSE* is lower than 0.5 g/kg and *COR* is ~77%, to be compared to ~1.1 g/kg and ~72% during the ChArMEx time periods. Below 2 km, the agreement is degraded as expected: RMSE is between ~2 and 3 g/kg and the COR value tends

238 to 0. Table 4 summarizes the results for different atmospheric layers between 0.5 and 7 km.
239 Such results are consistent with those of *Schneider and Hase* (2011) who used
240 rawinsoundings as validation tools for the IASI WVMR Level-2 operational products. With
241 the exception of the PBL, they found a correlation coefficient of ~0.80.

242 3.3 Water vapor integrated content

243 When considering the Water vapor integrated content (WVIC) between 0.5 and 7 km, the
244 agreement between lidar- and IASI-derived moisture is within a standard deviation between
245 0.18 and 0.25 g/cm^2. Figure 5 illustrates this agreement: the IASI-derived WVIC exhibits a
246 bias lower than 0.15 g/cm^2 compared to the one retrieved from WALI. In fact, the WVIC
247 retrieved from IASI is in the range value (between 0.5 and 2 g/cm^2) for the HyMeX time
248 period (fall 2012), but it is mostly underestimated by ~10% during the ChArMEx time period
249 (summer 2013). The slopes of the regressions are 0.89 and 0.81 for the HyMeX and
250 ChArMEx time periods, respectively. Note that during the HyMeX time period (fall 2012),
251 the agreement between the lidar and IASI profiles is better, even in the general shape.

252 When compared to ECMWF analyses, standard deviations with respect to WALI are close to
253 0.17 and 0.45 g/cm^2 for the two previous time periods, respectively. With respect to previous
254 IASI cross-comparisons, results are not degraded during the HyMeX fall period but
255 significantly worse over the ChArMEx summer period where the slope of the linear fit is
256 close to 0.70. Such discrepancy (underestimation) may be due to an incorrect consideration of
257 the instrumental error in the variance/covariance matrix needed for the assimilation process
258 (e.g. *Wang et al*., 2013). The error on the contribution to the IASI radiances may be linked to
259 local heating associated to the aerosol presence not being taken into account in the model, as
260 for all spaceborne infrared sensors (e.g. *Pierangélo et al*., 2004). This point is not within the
261 topic of this paper and has to be further investigated.

4 Influence of the air mass origins - aerosol as air mass tracer

Among all 30 coincidences, the origins of air masses are very different and can be characterized using simultaneously several aerosol optical properties and air mass back trajectories. The Raman lidar WALI offers the capability to retrieve fundamental aerosol optical properties (*Chazette et al.*, 2013): the vertical profiles of the volume depolarization ratio (VDR) to identify the presence of dust-like aerosols, the aerosol extinction coefficient (AE) to locate in altitude the scattering layers, the equivalent backscatter to extinction ratio (BER) which is proportional to the single scattering albedo, and the aerosol optical thickness (AOT) characterizing the aerosol column burden. The inversion process used both the N_2-Raman and elastic channels at 355 nm and is described in various papers as *Royer et al*. (2011) or *Chazette et al*. (2012) where the related uncertainties are assessed. Hence, using the aerosol optical properties described above, coupled with air mass back trajectory analysis, the air masses influencing the IASI-derived WVMR can be identified.

4.1 Aerosol optical properties

As in Figure 1, the dates of the relevant IASI coincidences are highlighted in white dotted lines in Figure 6. This figure represents the temporal evolution of the vertical profile of VDR for HyMeX and ChArMEx time periods, respectively. In general, the relevant coincidences do not occur during the major dust events where the VDR is maximal (in brown on the figure), likely because the dust plume is classified as cloud: it is sufficiently thick to significantly influence the brightness temperature used to inverse the IASI infrared spectrum. Nevertheless, other sources of aerosol may affect the IASI measurements. Thereby, the BER is also an important parameter to identify the aerosol types (e.g. *Cattrall et al*., 2005) as it is linked to their chemical composition. It is given in Figure 7 as a column average and presents a strong variability, ranging from ~0.01 sr^{-1} for pollution aerosol (e.g. *Raut and Chazette*, 2009) to ~0.04 sr^{-1} for marine aerosol (e.g. *Flamant et al*., 2000). The intermediate values are for

aerosol mixing, dust aerosols (e.g. *Mattis et al*., 2002; *Chazette et al*., 2007) or long-range transport pollution aerosols (e.g. *Chazette et al*., 2012). The AE and VDR vertical profiles are also given Figure 8 and Figure 9 for the coincidences of the two time periods. They often show strong heterogeneities with respect to altitude which are directly related to the vertical profiles of WVMR given Figure 2 and Figure 3, respectively. All the vertical structures encountered have to be investigated to compare the WVMR-derived from IASI and WALI. The aerosol atmospheric content in terms of AOT is also very different from one observation to another because it ranges from 0.04 (very clean air) to ~0.4 (polluted air and/or dust event). Hence, the coincidences are very diverse for an inter-comparison exercise, and allow evaluating the IASI-derived WVMR retrieval for very distinct atmospheric situations and aerosol contents.

4.2 Air mass back trajectories

Air mass back trajectories have been computed to determine the corresponding aerosol transport routes using the NOAA Hybrid Single Particle Lagrangian Integrated Trajectory (HYSPLIT) model (*Draxler and Rolph*, 2003) with 3-hourly archived meteorological data provided from the US National Centers for Environmental Prediction (NCEP) Global Data Assimilation System (GDAS) at the horizontal resolution of 0.5°. The altitudes of the trajectory starting points (1, 2 and 4 km) were selected primarily from the lidar observations of aerosol layer heights highlighted in Figure 8 and Figure 9. The air mass back trajectories are shown Figure 10, Figure 11 and Figure 12 for the 3 starting points and for each time period. One path was drawn on 72 hours for each coincidence between IASI and WALI measurements. The air mass origins are very variable during the time periods for all starting point altitudes. There are two major contributions to the air masses passing over Menorca, the first one from the Sahara and the second one from the Atlantic Ocean.

311 4.3 Discussion

312 The summary of our conclusion about the origins of air mass revealed by the shape of the
313 WVMR vertical profile is given in Table 2 and Table 3 for the HyMeX and ChArMEx time
314 periods, respectively. Depolarizing layers (DL) and residual pollution layers (RPL) are
315 specifically identified.

316 The atmospheric situations observed during the coincidences present significantly high
317 moisture content (WVMR > 5 g/kg in the free troposphere and WVIC close to 2 g/cm^2) for 4
318 (5) cases during the HyMeX (ChArMEx) time period, which correspond to *CN* = 1, 2, 6 and
319 10 (2, 5, 6, 7 and 8). Such situations are generally well represented by the Level-2 product of
320 the IASI operational ground segment, excepted for *CN* = 10 during the HyMeX time period
321 where the IASI product overestimates the WVMR by ~25%. In this case, the air mass came
322 from Morocco and brought moisture with dust aerosols between ground and ~4 km above the
323 mean sea level (amsl). Nevertheless, it must be noted that Saharan air masses are often
324 associated with higher moisture content and the agreement between IASI- and WALI-derived
325 WVMR is generally better for these air masses because of the smoother transitions in vertical
326 structures due to higher moisture content in these layers.

327 The major discrepancies are observed for the drier air masses (WVIC less or close to 1 g/cm^2)
328 which present a strong vertical gradient of WVMR, generally between the PBL and the free
329 troposphere. Such a gradient is not reproduced from IASI measurements due to its insufficient
330 vertical resolution. Note that the dry air masses observed during the field campaigns
331 originated from the Atlantic and had a small AOT (< 0.2).

332 For the other coincidences, the agreement between IASI and WALI is good. The median
333 value of the atmospheric aerosol content (*AOT* ~ 0.2) is similar during the two time periods
334 and cannot explain the observed differences between them. During the ChArMEx time period

several coincidences are associated with very clean air (*AOT* < 0.1) situations. Furthermore, the differences observed in the WALI/ECMWF comparison cannot be explained by the presence of an aerosol layer. These discrepancies seem linked to a seasonal role, which could be due to an incorrect consideration of the sea surface temperature in the model.

The air mass origin plays a major role through the shape of the original vertical structure which can be kept during several days along the transport. As discussed by *Kim et al*. (2004), the larger amount of water vapor in an aerosol layer contributes to a higher radiative heating, increasing the potential temperature and static stability of the layer. This may help to maintain the structure of the layer for a longer period of time. Note that the vertical structures observed during our two field campaigns are not uncommon in the atmosphere (e.g. *Chazette et al*., 2001; *Kim et al*., 2009). All this suggests a need for an increased vertical resolution of infrared spaceborne sounders, and then for the improvement of their spectral resolution (e.g. *Crevoisier et al*., 2013b).

5 Conclusion

Following the international field campaigns HyMeX and ChArMEx in fall 2012 and summer 2013, respectively, 30 relevant coincidences between the ground-based lidar WALI and the spaceborne instrument IASI have been selected to conduct a comparison exercise of the WVMR vertical profile retrieval. The general result is in good agreement between the two instruments. Two statistical indicators generally used to evaluate model performances have been considered: the Root Mean Square Error (RMSE) and the (Pearson) correlation (COR). In the middle troposphere (2-7 km amsl) the COR value is ~77 and 72%, and the RMSE is lower than 0.5 and 1.1 g/kg for the fall and summer periods, respectively. Discrepancies are higher in the PBL because the weighted functions of IASI do not correctly sample this layer close to the ground (*RMSE* ~ 1.6 g/kg and *COR* < 0.4). Considering the water vapor integrated

359 content within the altitude range of 0.3 and 7 km amsl, the standard deviation between IASI
360 and WALI are 0.18 and 0.25 g/cm^2 for the fall and summer periods, respectively. The
361 disagreement is higher during summer time and we may suspect the presence of aerosol layers
362 and/or contrasted vertical atmospheric structures to be responsible for this bias.

363 During coincidences, we note that the integrated atmospheric aerosol content has been found
364 with aerosol optical thickness between 0.04 and 0.4 associated with various particle types
365 (pollution, marine or dust aerosols), as identified from both the lidar-derived backscatter to
366 extinction ratio and air mass back trajectories. The aerosol optical thickness does not
367 significantly affect the results of the intercomparison. The divergence on the WVMR vertical
368 profile is mainly due to the existence of sharp transitions which mainly occurs between the
369 PBL and the free troposphere. The agreement is generally better for Saharan air masses
370 because of the smoother transitions in vertical structures due to higher moisture content in
371 these layers (~5 g/kg). Our results calls for an improvement of the spectral resolution of the
372 Fourier transform spectrometer IASI. Such consideration is being studied for the next
373 generation, the so-called IASI-NG. Moreover, the synergetic use of microwave measurements
374 is capable of improving the water vapor retrievals, especially in the PBL. An upcoming
375 version (6) of the operational IASI Level 2 processor with synergistic use of the Advanced
376 Microwave Sounding Unit (AMSU) and the Microwave Humidity Sounder (MHS) data is
377 scheduled. It was reported to contain substantial improvements of the profiles when compared
378 with ECMWF analysis, in particular in the lower levels and for the entire water vapor profiles.
379 The approach presented in this study can be applied to the next generation of IASI operational
380 water vapor products.

381 **Acknowledgments.** This work was supported by the French Agence Nationale de la
382 Recherche (ANR) via the HyMeX /IODA-MED project, the French space agency (CNES) and

the Commissariat à l'Energie Atomique (CEA). We also thank M. Sicard and F. Dulac for their help for installing the lidar station on the Menorca Island. ECMWF data used in this study have been obtained from the ECMWF Data Server. The authors would additionally like to thank the HyMeX and ChArMEx programs for their support. The IASI Level-2 Water Vapor Mixing Ratio profiles used in this paper are Courtesy Ether CNES/CNRS-INSU Ether web site http://www.pole-ether.fr.

6 References

Amato, U., Antoniadis, A., De Feis, I., Masiello, G., Matricardi, M., and Serio, C.: Technical Note: Functional sliced inverse regression to infer temperature, water vapour and ozone from IASI data, *Atmos. Chem. Phys*., *9*, 5321-5330, doi:10.5194/acp-9-5321-2009, 2009.

Aumann, H.H., and Miller, C.: Atmospheric Infrared Sounder (AIRS) on the Earth Observing System, in Advanced and next-generation satellite, H. Fujisada and M.N. Sweeting, eds., Proc. SPIE 2583, 332-338, 1995.

August, T., Klaes, D., Schlussel, P., Hultberg, T., Crapeau, M., Arriaga, A., O'Carroll, A., Coppens, D., Munro, R., and Calbet, X.: IASI on Metop-A:Operational Level 2 retrievals after five years in orbit, *Journal of Quantitative Spectroscopy & Radiative Transfer*, *113*, 1340–1371, 2012.

Bormann, N., Collard, A., and Bauer, P.: Estimates of spatial and interchannel observation-error characteristics for current sounder radiances for numerical weather prediction. II: Application to AIRS and IASI data, *Q. J. Roy. Meteorol. Soc*., *136*, 1051-1063, 2010.

Boylan, J. W. and Russell, A. G.: PM and light extinction model performance metrics, goals, and criteria for three-dimensional air quality models, *Atmos. Environ.*, *40*, 4946–4959, 2006.

Carissimo, A., De Feisi, I., and Serio, C.: The physical retrieval methodology for IASI: the -IASI code, *Environ. Modell. Softw*., *20*, 9, 1111–1126, doi:10.1016/j.envsoft.2004.07.003, 2005.

Cattrall, C., Reagan, J., Thome, K., and Dubovik, O.: Variability of aerosol and spectral lidar and backscatter and extinction ratios of key aerosol types derived from selected Aerosol Robotic Network locations, *J. Geophys. Res.*, *110*, D10S11, doi:10.1029/2004JD005124, 2005.

Cayla, F-R.: IASI infrared interferometer for operations and research. In: Chedin A, Chahine MT, Scott NA, editors. High spectral resolution infrared remote sensing for Earth's weather and climate studies, NATO ASI series, vol. I 9. Berlin: Springer Verlag, 1993.

Chahine, M.T., O'Callaghan, F.G., Aumann, H.H., Capps, R.W., Haskins, R.D., Pagano, R.J., and Schlindler, R.A.: Atmospheric Infrared Sounder (AIRS)-Science and measurement requirements, NASA-TM-104977, Washington D.C., 36 pp, 1990.

Chazette, P., Clerbaux, C., and Mégie, G.: Radiative forcing of methane estimated using nadir spectral radiances, *Appl. Opt*., *37*, 15, 3113-3120, 1998.

Chazette, P., Pelon, J., Moulin, C., Dulac, F., Carrasco, I., Guelle, W., Bousquet, P., and Flamant, P.H.: Airborne lidar and Meteosat synergy to characterize a Saharan dust plume over the Azores during SOFIA/ASTEX, *Atmos. Environ*., *35*, 4297-4304, 2001.

Chazette, P., Sanak, J., and Dulac, F.: New Approach for Aerosol Profiling with a lidar Onboard an Ultralight Aircraft: Application to the African Monsoon Multidisciplinary Analysis, *Environ. Sci. Technol.*, *41*, 8335–8341, 2007.

Chazette, P., Bocquet, M., Royer, P., Winiarek, V., Raut, J.-C., Labazuy, P., Gouhier, M., Lardier, M., and Cariou, J.-P.: Eyjafjallajökull ash concentrations derived from both lidar and modeling, *J. Geophys. Res.*, *117*, D00U14, doi:10.1029/2011JD015755, 2012.

Chazette, P., Marnas, F., and Totems, J.: The mobile Water vapor Aerosol Raman lidar and its implication in the frame of the HyMeX and ChArMEx programs: application to a dust transport process, *Atmos. Meas. Tech. Discuss.*, *6*, 10653-10698, doi:10.5194/amtd-6-10653-2013, 2013.

Chedin, A., Scott, N. A., Wahiche, C., and Moulinier, P.: The improved initialization inversion method: a high resolution physical method fo temperature retrievals from satellites of the TIROS-N series, *J. Climate Appl. Meteorol.*, *24*, doi:10.1175/1520-0450(1985)024, 128:143, 1985.

Clerbaux, C., Chazette, P., Hadji-Lazaro, J., Müller, J.F., Clough, T., and Mégie, G.: Remote sensing of O_3, CO and CH_4 using a spaceborne nadir-viewing instrument, *J. Geophys. Res.*, *103*, D15, 18999-19013, 1998.

Clerbaux, C., Boynard, A., Clarisse, L., George, M., Hadji-Lazaro, J., Herbin, H., Hurtmans, D., Pommier, M., Razavi, A., Turquety, S., Wespes, C., and Coheur, P.-F.: Monitoring of atmospheric composition using the thermal infrared IASI/MetOp sounder, *Atmos. Chem. Phys.*, *9*, 6041–6054, doi:10.5194/acp-9-6041-2009, 2009.

Collard, A.D., and McNally, A.P.: The assimilation of Infrared Atmospheric Sounding Interferometer radiances at ECMWF, *Q. J. Roy. Meteorol. Soc.*, *135*, 1044-1058, 2009.

Crevoisier, C., Nobileau, D., Armante, R., Crépeau, L., Machida, T., Sawa, Y., Matsueda, H., Schuck, T., Thonat, T., Pernin, J., Scott, N. A., and Chédin, A.: The 2007–2011 evolution of tropical methane in the mid-troposphere as seen from space by MetOp-A/IASI, *Atmos. Chem. Phys.*, *13*, 4279-4289, doi:10.5194/acp-13-4279-2013, 2013a.

Crevoisier, C., Clerbaux, C., Guidard, V., Phulpin, T., Armante, R., Barret, B., Camy-Peyret, C., Chaboureau, J.-P., Coheur, P.-F., Crépeau, L., Dufour, G., Labonnote, L., Lavanant, L., Hadji-Lazaro, J., Herbin, H., Jacquinet-Husson, N., Payan, S., Péquignot, E., Pierangelo, C., Sellitto, P., and Stubenrauch, C.: Towards IASI-New Generation (IASI-NG): impact of improved spectral resolution and radiometric noise on the retrieval of thermodynamic, chemistry and climate variables, *Atmos. Meas. Tech. Discuss.*, *6*, 11215-11277, doi:10.5194/amtd-6-11215-2013, 2013b.

Draxler, R.R., and Rolph, G.D.: HYSPLIT (HYbrid Single-Particle Lagrangian Integrated Trajectory) Model access via NOAA ARL READY Website

(http://www.arl.noaa.gov/ready/hysplit4.html). NOAA Air Resources Laboratory, Silver Spring, MD, 2003.

Flamant C., Pelon, J., Chazette, P., Trouillet, V., Quinn, P., Frouin, R., Bruneau, D., Léon, J.F., Bates, T., Johnson, J., and Livingston, J.: Airborne lidar measurements of aerosol spatial distribution and optical properties over the Atlantic Ocean during an European pollution outbreak of ACE-2, *Tellus*, *52B*, 662-667, 2000.

Grieco, G., Masiello, G., Matricardi, M., and Serio, C.: Partially scanned interferogram methodology applied to IASI for the retrieval of CO, CO2, CH4 and N2O, *Opt. Express*, *21*, 24753-24769; doi: 10.1364/OE.21.024753, 2013.

Griffin, D., Walker, K. A., Franklin, J. E., Parrington, M., Whaley, C., Hopper, J., Drummond, J. R., Palmer, P. I., Strong, K., Duck, T. J., Abboud, I., Bernath, P. F., Clerbaux, C., Coheur, P.-F., Curry, K. R., Dan, L., Hyer, E., Kliever, J., Lesins, G., Maurice, M., Saha, A., Tereszchuk, K., and Weaver, D.: Investigation of CO, C_2H_6 and aerosols in a boreal fire plume over eastern Canada during BORTAS 2011 using ground- and satellite-based observations and model simulations, *Atmos. Chem. Phys*., *13*, 10227-10241, doi:10.5194/acp-13-10227-2013, 2013.

Heilliette S., Y. J. Rochon, L. Garand, and J. W. Kaminski: Assimilation of Infrared Radiances in the Context of Observing System Simulation Experiments *Journal of Applied Meteorology and Climatology*, *52*(4), 1031-1045, doi:10.1175/JAMC-D-12-0124.1, 2013.

Held, I.M., and Soden, B.J.: Water vapor feedback and global warming, Annual Rev. Energy Environ., 25, 441-475, DOI: 10.1146/annurev.energy.25.1.441, 2000.

Hilton, F., Atkinson, N.C., English, S.J., and Eyre, J.R.: Assimilation of IASI at the Met Office and assessment of its impact through observing system experiments, *Q. J. Roy. Meteorol. Soc*., *135*, 495-505, 2009.

Hilton, F., Armante, R., August, T., Barnet, C., Bouchard, A., Camy-Peyret, C., Capelle, V., Clarisse, L., Clerbaux, C., Coheur, P.-F., Collard, A., Crevoisier, C., Dufour, G., Edwards, D., Faijan, F., Fourrié, N., Gambacorta, A., Goldberg, M., Guidard, V., Hurtmans, D., Illingworth, S., Jacquinet-Husson, N., Kerzenmacher, T., Klaes, D., Lavanant, L., Masiello, G., Matricardi, M., McNally, A., Newman, S., Pavelin, E., Payan, S., Péquignot, E., Peyridieu, S., Phulpin, T., Remedios, J., Schlüssel, P., Serio, C., Strow, L., Stubenrauch, C., Taylor, J., Tobin, D., Wolf, W., and Zhou, D.: Hyperspectral Earth Observation from IASI: Five Years of Accomplishments, *Bull. Am. Meteorol. Soc.*, *93*, 347–370, DOI: 10.1175/BAMS-D-11-00027.1, 2012.

IPCC: Climate Change 2013: The physical science basis. Contribution of working group I to the fifth assessment report of the Intergovernmental Panel on Climate Change [Stocker, T.F., D. Qin, G.-K. Plattner, M. Tignor, S.K. Allen, J. Boschung, A. Nauels, Y. Xia, V.

498 Bex and P.M. Midgley (eds.)]. Cambridge University Press, Cambridge, United Kingdom
499 and New York, NY, USA, 1535 pp., 2013.

500 Kim, S-W., Yoon, S-C., Jefferson, A., Won, J-G., Dutton, E.G., Ogren, J.A., and Anderson,
501 T.L.: Observation of enhanced water vapor in Asian dust layer and its effect on
502 atmospheric radiative heating rates, *Geophy. Res. Letters*, *31*, L18113,
503 doi:10.1029/2004GL020024, 2004.

504 Kim, S.-W., Chazette, P., Dulac, F., Sanak, J., Johnson, B., andYoon, S.-C.: Transport and
505 vertical structure of aerosols and water vapor over West Africa during the African
506 monsoon dry season, *Atmos. Chem. Phys.*, *9*, 8017-8038, 2009.

507 Klaes, K.D.,Cohen, M., Buhler, Y., Schussel, P., Munro, R., von Engeln, A., Clérigh, E.,
508 Bonekamp, H, Ackermann, J., and Schmetz, J.: An introduction to the EUMETSAT polar
509 system, *Bull. Am. Meteorol. Soc*., *88*, 1085–96, doi:10.1175/BAMS-88-7-1085, 2007.

510 Larson, T.V., and Taylor, G.S.: On the evaporation of NH4NO3 aerosol, *Atmos. Environ*., *17*,
511 2489-2595, 1983.

512 Masiello, G., Serio, C., Deleporte, T., Herbin, H., Di Girolamo, P., Champollion, C.,
513 Behrendt, A., Bosser, P., Bock, O., Wulfmeyer, V., Pommier, M., and Flamant, C.:
514 Comparison of IASI water vapour products over complex terrain with COPS campaign
515 data, *Meteorologische Zeitschrift*, *22*, 4, 471-487, doi:10.1127/0941-2948/2013/0430,
516 2013.

517 Matricardi, M., and McNally, A. P.: The direct assimilation of principal components of IASI
518 spectra in the ECMWF 4D-Var, *Q. J. Roy. Meteor. Soc*., *140*, 573-582,
519 doi:10.1002/qj.2156, 2013.

520 Mattis, I., Ansmann A., Müller D., Wandinger U., and Althausen D., Dual-wavelength Raman
521 lidar observations of the extinction-to-backscatter ratio of Saharan dust, Geophys. Res.
522 Lett., 29, 9, 1306, doi:10.1029/2002GL014721, 2002.

523 Ogawa, T., Shimoda, H., Hayashi, M., Imasu, R, Ono, A, Nishinomiya, S, and Kobayashi, H:
524 IMG, Interferometric measurement of greenhouse gases from space, *Adv. Space. Res.*, *14*,
525 25-28, 1994.

526 Pierangélo, C., Chedin, A., and Chazette, P.: Measurements of Stratospheric Volcanic Aerosol
527 Optical Depth from NOAA/TOVS Observations, *J. Geophys. Res*., *109*, D03207, 2004.

528 Pougatchev, N., August, T., Calbet, X., Hultberg, T., Oduleye, O., Schlüssel, P., Stiller, B.,
529 Germain, K. St., and Bingham, G.: IASI temperature and water vapor retrievals – error
530 assessment and validation, *Atmos. Chem. Phys*., *9*, 6453-6458, doi:10.5194/acp-9-6453-
531 2009, 2009.

Randriamiarisoa, H., Chazette, P., Couvert, P., and Sanak, J.: Relative humidity impact on aerosol parameters in a Paris suburban area, *Atmos. Chem. Phys.*, *6*, 1389–1407, doi:10.5194/acp-6-1389-2006, 2006.

Raut, J.-C., and Chazette, P.: Assessment of vertically-resolved PM_{10} from mobile lidar observations, Atmos. Chem. Phys., 9, 8617-8638, doi:10.5194/acp-9-8617-2009, 2009.

Rood, M.J., Covert, D.S., and Larson, T.V.: Hygroscopic properties of atmospheric aerosol in Riverside, California, *Tellus*, *39B*, 383-397, 1987.

Royer, P., Chazette, P., Lardier, M., and Sauvage, L.: Aerosol content survey by mini-N2-Raman lidar: Application to local and long-range transport aerosols, *Atmos. Environ*., doi:10.1016/j.atmosenv.2010.11.001, 2011.

Schneider, M., and Hase, F.: Optimal estimation of tropospheric H2O and δD with IASI/METOP, *Atmos. Chem. Phys.*, *11*, 11207-11220, doi:10.5194/acp-11-11207-2011, 2011.

Schlüssel, P., Hultberg, T., Phillips, P., August, T. and Calbet, X.: The operational IASI Level 2 processor, *Adv. Space Res*., *36*, 982-988, 2005.

Shephard, M.W, Herman, R.L., Fisher, B.M., Cady-Pereira, K.E., Clough, S.A., Payne, V.H., Whiteman, D.N., Comer, J.P., Vömel, H., Miloshevich, L.M., Forno, R., Adam, M., Osterman, G.B., Eldering, A., Worden, J.R., Brown, L.R., Worden, H.M., Kulawik, S.S., Rider, D.M., Goldman, A., Beer, R., Bowman, K.W., Rodgers, C.D., Luo, M., Rinsland, C.P., Lampel, M., and Gunson, M.R.: Comparison of Tropospheric Emission Spectrometer Nadir Water Vapor Retrievals with *In Situ* Measurements, *J. Geophys. Res.*, *113*, D15S24, doi:10.1029/2007JD008822, May 16, 2008.

Susskind, J., Rosenfield, J., Reuter, D., and Chahine, M.T.: Remote sensing of weather and climate parameters from HIRS2/MSU on TIROS-N. *J. Geophys. Res.*, *89*, 4677-4697, 1984.

Wang, Y., Sartelet, K. N., Bocquet, M., and Chazette, P.: Modelling and assimilation of lidar signals over Greater Paris during the MEGAPOLI summer campaign, *Atmos. Chem. Phys. Discuss*., *13*, 27115-27161, doi:10.5194/acpd-13-27115-2013, 2013.

Worden, J., Kulawik, S., Frankenberg, C., Payne, V., Bowman, K., Cady-Peirara, K., Wecht, K., Lee, J.-E., and Noone, D.: Profiles of CH_4, HDO, H_2O, and N_2O with improved lower tropospheric vertical resolution from Aura TES radiances, *Atmos. Meas. Tech*., *5*, 397-411, doi:10.5194/amt-5-397-2012, 2012.

Xu, D., Liu Z., Zhiquan, Huang, X.-Y., Min, J., and Wang, H.: Impact of assimilating IASI radiance observations on forecasts of two tropical cyclones, Meteorology and Atmospheric Physics, 122, 1-18, doi: 10.1007/s00703-013-0276-2, 2013.

567 Zhou, D. K., Smith, W. L., Larar, A. M., Liu, X., Taylor, J. P., Schlüssel, P., Strow, L. L., and
568 Mango, S. A.: All weather IASI single field-of-view retrievals: case study – validation with
569 JAIVEx data, *Atmos. Chem. Phys.*, *9*, 2241-2255, doi:10.5194/acp-9-2241-2009, 2009.

570

571

572 Table 1: Main technical characteristics of the WALI instrument.

Laser	Nd:Yag
Energy	60 mJ at 355 nm
Frequency	20 Hz
Reception channels	Elastic total 354.67 nm Elastic ⊥ 354.67 nm Raman-N_2 386.63 nm Raman-H_2O 407.5 nm
Reception diameters	15 cm
Field of view	~2.3 mrad
Full overlap	~300 m
Detector	Photomultiplier tubes
Filter bandwidths	0.2 - 0.3 nm
Vertical sampling	0.75 m (analog) 15 m (photon counting)
Vertical resolution used for this study	~ 40 m
Acquisition system	PXI technology at 200 MHz

573

574 Table 2: List of the coincidence numbers (CN) and description of the associated aerosol layer
575 synoptic origin during the HyMeX experiment (2012 fall period). *D* represents the distance
576 between the ground-based lidar and the center of the 12 selected IASI pixels. *N* is the number
577 of available averaged IASI profiles. The wettest (driest) coincidences are in bold (italic). The
578 presences of dry layer (DL) and residual particle layer (RPL) are indicated.

(CN) Month/Day - LT	*D* (km)	*N*	Observation
(1) **09/19 - 23:03**	0.6	8	Atlantic-Spain origin, RPL below 2 km DL between 3 and 4 km, air mass off Eastern African coast
(2) **09/20 - 22:42**	2.4	12	Atlantic - Spain origin DL between 2 and 4 km, air mass along Eastern African coast Subsidence between ~0 and 3 km above Southern Spain
(3) 09/22 - 21:59	19.3	12	Saharan origin between 1 and 5 km (Algeria-Morocco) DL between 1 and 4 km, air mass along Eastern African coast Strong ascent from ~0 to 3 km above Morocco
(4) *09/24 - 22:59*	2.8	6	Atlantic - Spain origin with a RPL below 1.5 km (from Valencia) Strong subsidence from ~4 to 0 km
(5) *09/25 - 22:39*	3.9	12	Atlantic-Southern Spain origin Below 1 km, RPL from Gibraltar with strong subsidence from ~3 km
(6) **09/30 - 22:33**	55.2	6	Between 2 and 5 km, Saharan, France and Spain origin Below 1 km, RPL from Gibraltar (petrochemistry) Strong subsidence from 8 to 4 km above Moroccan sea coast
(7) 10/01 - 22:15	8.3	11	Northern Spain - Southwestern France origin RPL below 3 km from Valencia-Barcelona
(8) *10/03 - 23:12*	5.2	12	Spain origin RPL below 2 km from Valencia coast
(9) 10/04 - 22:51	2.6	12	Saharan (Morocco) and Southern - Spain origin DL between 2 and 4 km
(10) **10/08 - 23:09**	2.1	9	Tropical Atlantic - Spain origin DL below 4 km, mainly between 2 and 4 km May be Saharan air masses off African west coast
(11) 10/09 - 22:48	6.5	12	Tropical Atlantic - Spain origin Below 2 km, RPL from Valencia-Barcelona coast
(12) 10/13 - 23:06	8.5	11	Atlantic - Northern Spain origin RPL from Barcelona coast
(13) 10/16 - 22:03	45.8	6	Atlantic-Spain origin Strong subsidence from 4 to 1 km over Spain RPL from Valencia-Barcelona coast
(14) 10/17 - 23:24	5.2	11	Saharan origin with a strong DL below 3 km Strong subsidence from 4 to 0 km over Sahara
(15) 10/23 - 22:57	3.3	9	Spain origin - Long passage over the Mediterranean sea No significant aerosol layer

579

580 Table 3: Same as Table 2 for the ChArMEx experiment (2013 summer period).

(CN) Month/Day - LT	*D* (km)	*N*	Observation
(1) 06/10 - 21:59	5.8	12	Spain - Southern France origin Strong subsidence from ~6 to 2 km
(2) **06/11 - 23:18**	7.2	12	Atlantic - Spain origin RPL from Barcelona coast
(3) 06/12 - 22:57	3.5	12	Atlantic - Spain origin Strong subsidence from ~8 to 5 km
(4) 06/13 - 22:36	5.0	12	Atlantic-Southern France origin RPL from Perpignan coast Dry air mass at ~3 km (drying over the Pyrenees)
(5) **06/14 - 22:15**	2.2	12	France origin below 1 km Tropical Atlantic - Southern Spain origin above 1 km RPL from Valencia coast
(6) **06/15 - 21:54**	4.4	12	Mediterranean origin below 1 km Atlantic (off Moroccan coast) - Southern Spain origin above 1 km DL between ~2.5 and 4 km
(7) **06/16 - 23:15**	11.2	12	Mediterranean origin below 1 km Morocco-Algeria origin above 1 km DL between 1 and 5 km
(8) **06/17 - 22:54**	4.0	10	Atlantic - Morocco origin with a small DL ~0-7 km. Likely dust uptake between 0 and 4 km
(9) 06/20 - 23:33	47.1	12	Spain origin RPL from Valencia coast
(10) 06/22 - 22:51	3.0	12	Atlantic - Spain - Southwestern France origin Strong subsidence between ~9 and 4 km RPL from Barcelona coast
(11) *06/24 - 22:09*	8.2	12	Atlantic - Spain - Southwestern France origin Strong subsidence between ~7 and 0 km Dry air mass at ~2.5 km RPL from Barcelona coast
(12) 06/25 - 23:27	29.0	12	Atlantic - Spain - Southwestern France origin Strong subsidence between ~8 and 4 km RPL from Perpignan coast
(13) *06/27 - 22:48*	14.3	6	Northern Atlantic - France origin RPL from Perpignan coast
(14) 06/30 - 23:24	19.4	12	Northwestern Atlantic - France origin
(15) 07/02 - 22:42	4.2	10	France - Spain - Morocco origin with a DL between 3 and 5 km Strong wind-shear - RPL from Montpellier and Barcelona coasts

581

582 Table 4: Scores on the WVMR retrieval for the inter-comparisons between WALI and IASI
583 (WALI-IASI), and WALI and ECMWF (WALI-ECMWF). The results are given for different
584 atmospheric layers in terms of COR and RMSE for the two time periods.

Altitude range (km)	COR		RMSE (g/kg)	
September-October 2012				
	WALI-IASI	WALI-ECMWF	WALI_IASI	WALI-ECMWF
0.5-2.0	0.37	0.73	1.42	1.15
2.0-5.0	0.77	0.81	0.66	0.55
5.0-7.0	0.78	0.73	0.25	0.26
0.5-7.0	0.70	0.77	0.78	0.65
June-July 2013				
	WALI-IASI	WALI-ECMWF	WALI_IASI	WALI-ECMWF
0.5-2.0	0.15	0.74	1.80	2.42
2.0-5.0	0.70	0.91	1.34	1.16
5.0-7.0	0.75	0.77	0.67	0.66
0.5-7.0	0.59	0.82	1.28	1.43

585

586

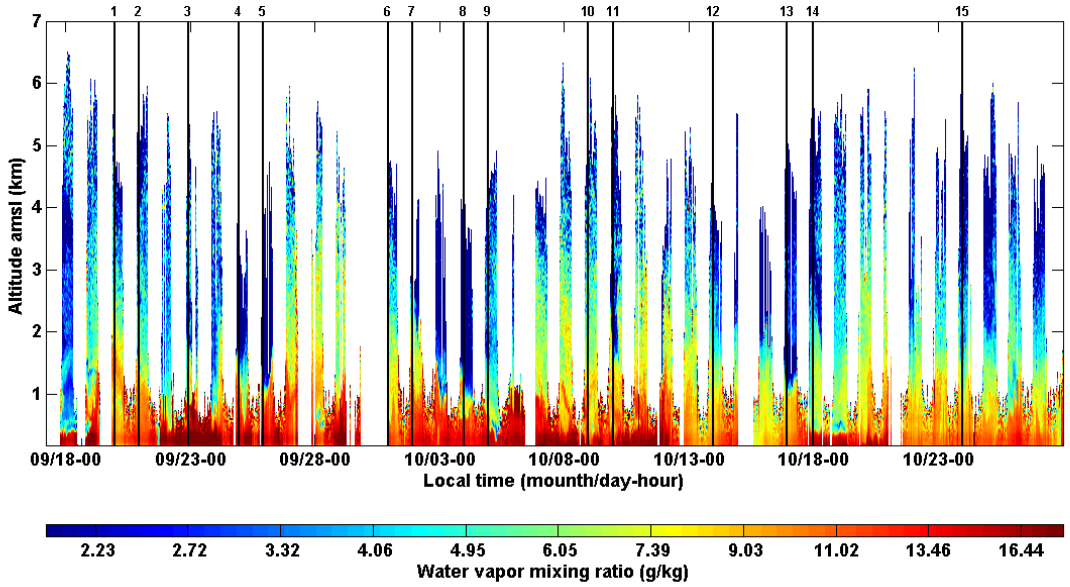

587

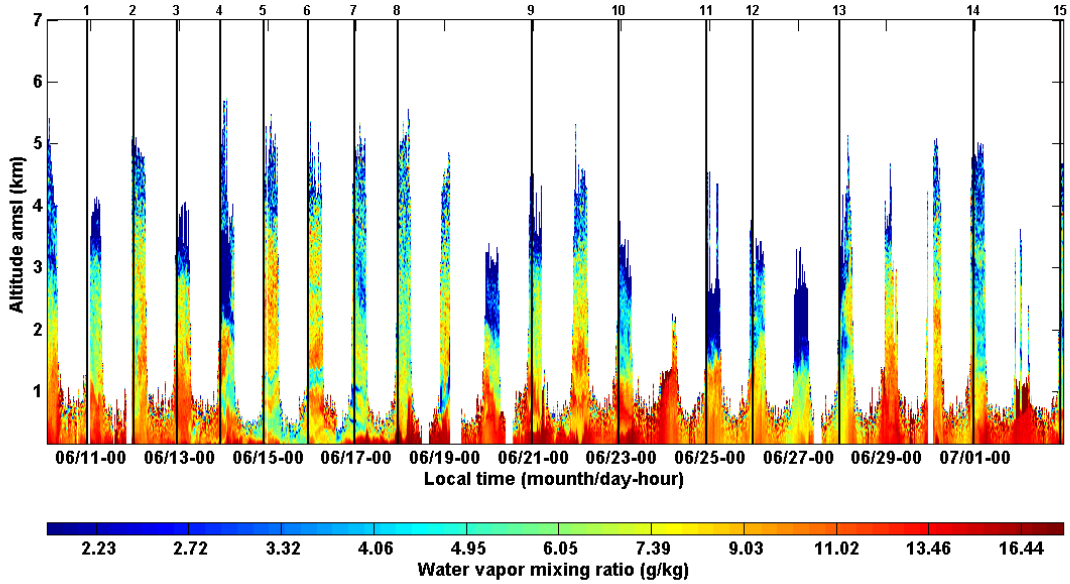

588

589 Figure 1: Time localization of the IASI profiles used for the inter-comparisons (vertical black
590 lines identified with the CN at the top) with respect to the temporal WALI lidar WVMR (in
591 g/kg) retrieval evolution as a function of altitude (in km) during the HyMeX (up) and
592 ChArMEx (down) periods. lidar profiles are given with a high temporal resolution of 5
593 minutes averaging. The color bar ranges from low water vapor mixing-ratio (blue) to high
594 ones (red).

595

596

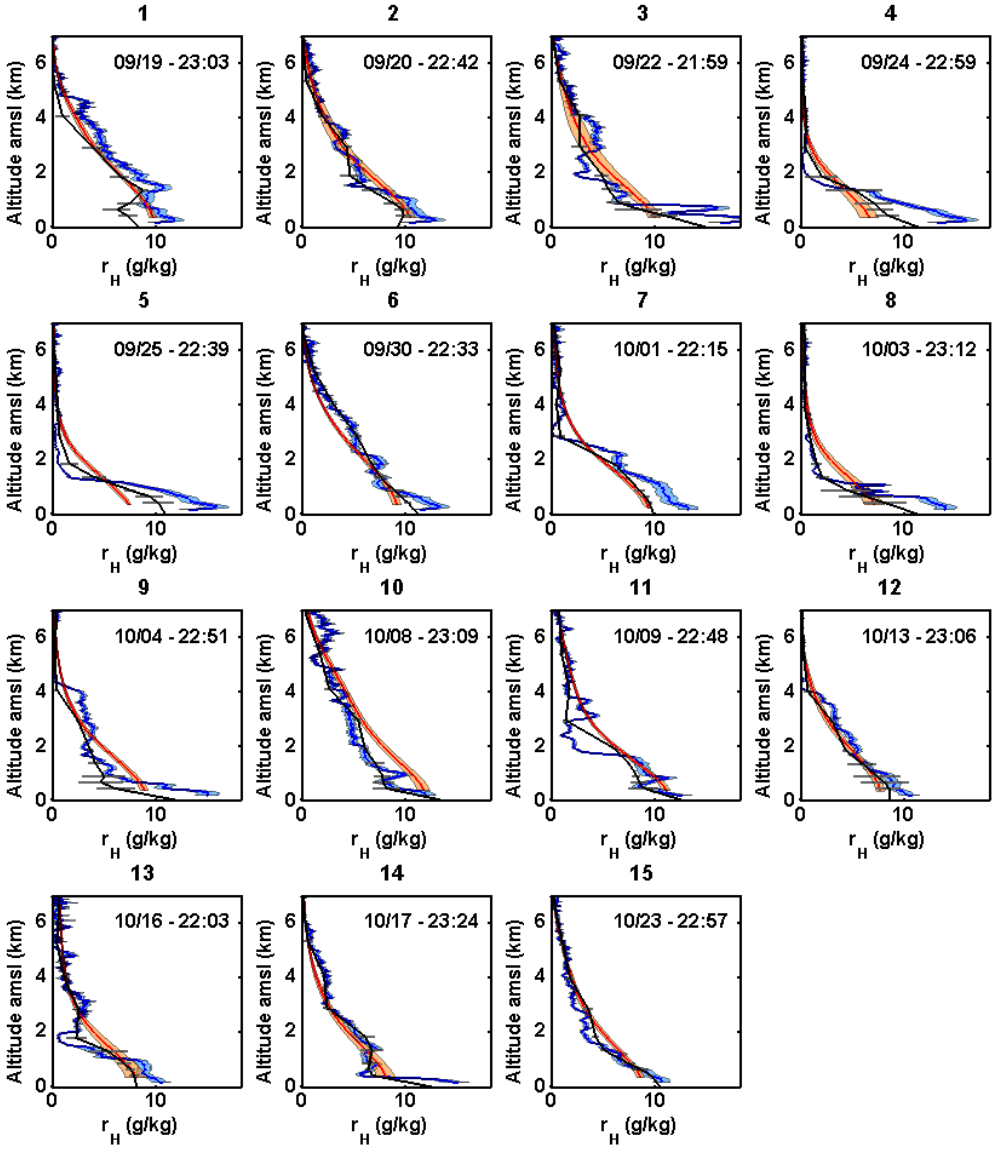

597

598 Figure 2: Comparisons of WVMR vertical profile retrieval as a function of altitude between:
599 IASI (red), WALI lidar (blue) and ECMWF analysis (black), over Menorca during the
600 HyMeX experiment (September and October 2012). The date and time of the IASI and WALI
601 measurements are also given for each panel of individual profile in the form month/day
602 HH:MM. The CN is given at the top of each figure.

603

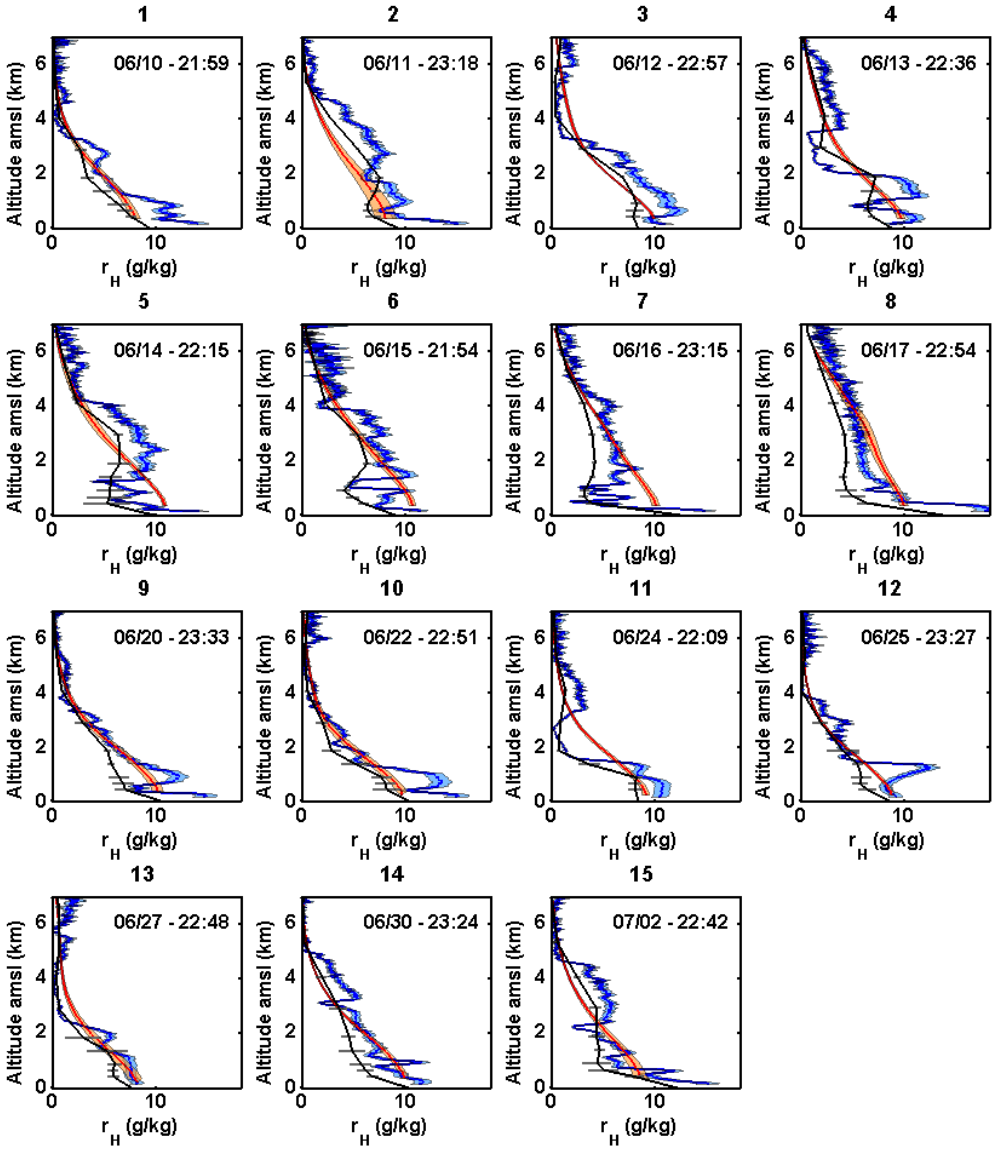

604

605 Figure 3: Same as Figure 2 for the ChArMEx experiment (June and July 2013).

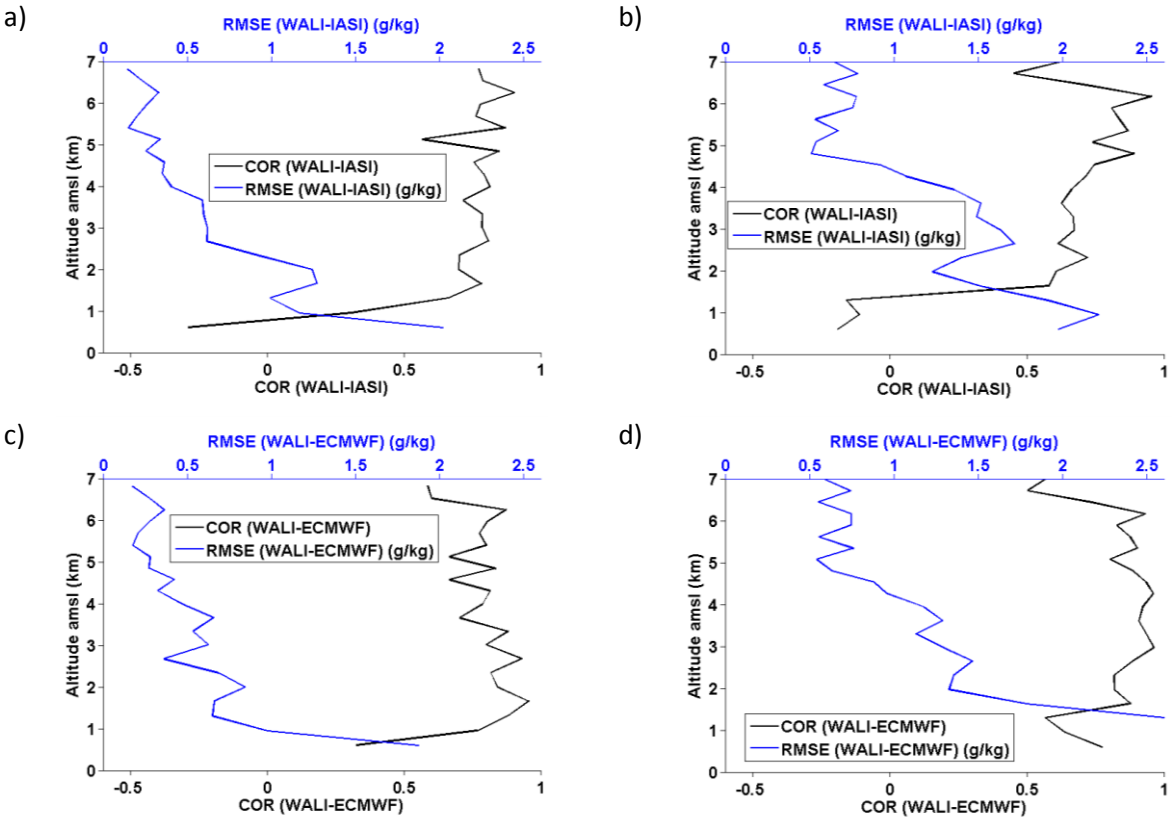

606 Figure 4: Evolution as a function of altitude of the RMSE in g/kg (blue) and COR between
607 IASI and WALI WVMR retrievals for HyMeX (a) and ChArMEx (b) periods, and between
608 WALI WVMR retrieval and ECMWF analysis for HyMeX (c) and ChArMEx (d) periods.

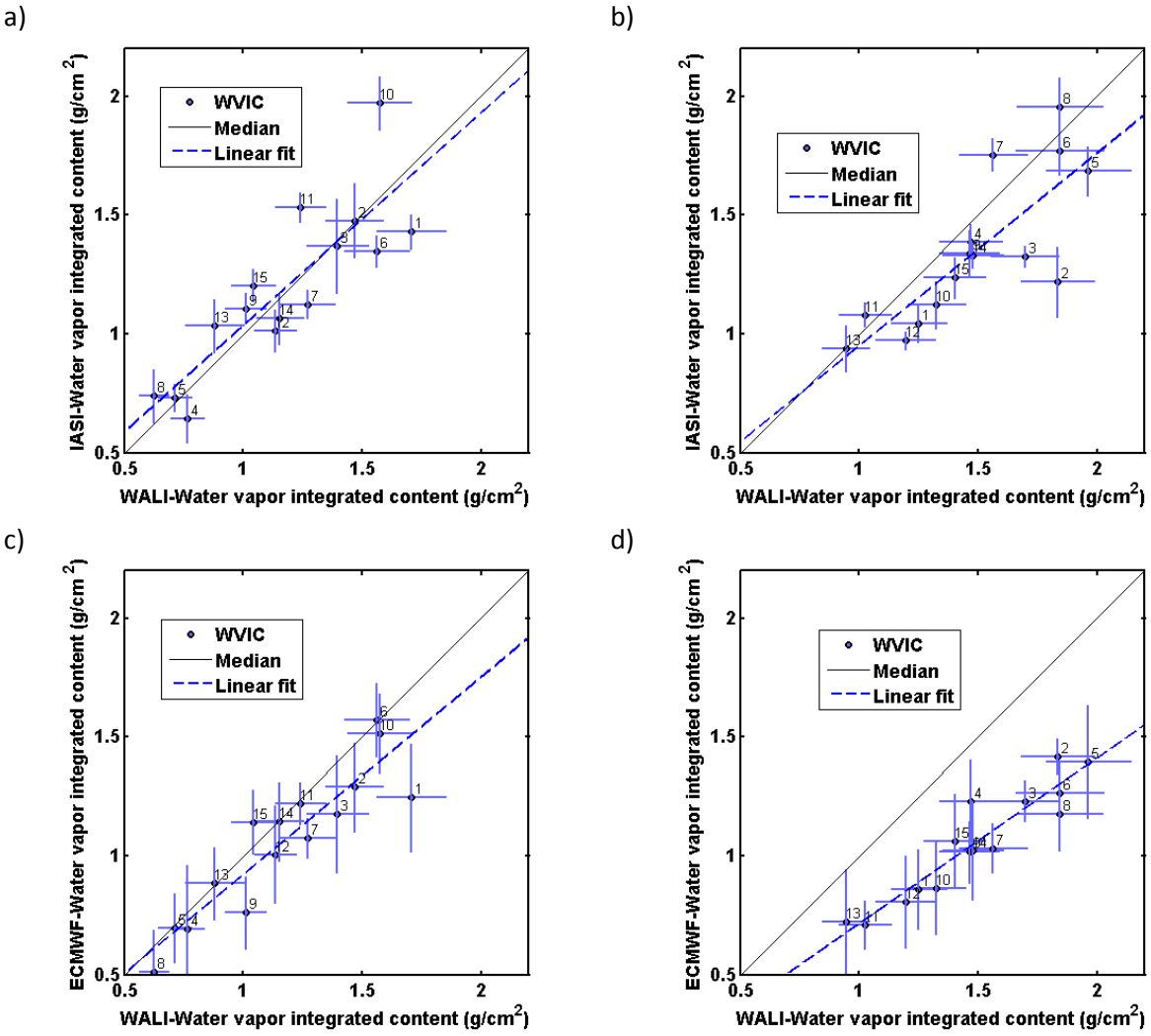

609

610 Figure 5: Water Vapor Integrated Content (WVIC in g/cm^2) as measured by WALI lidar
611 against IASI WVIC retrieval for HyMeX (a) and ChArMEx (b) periods and against ECMWF
612 WVIR for HyMeX (c) and ChArMEx periods (d). Line styles are given in each individual
613 figure legends.

614

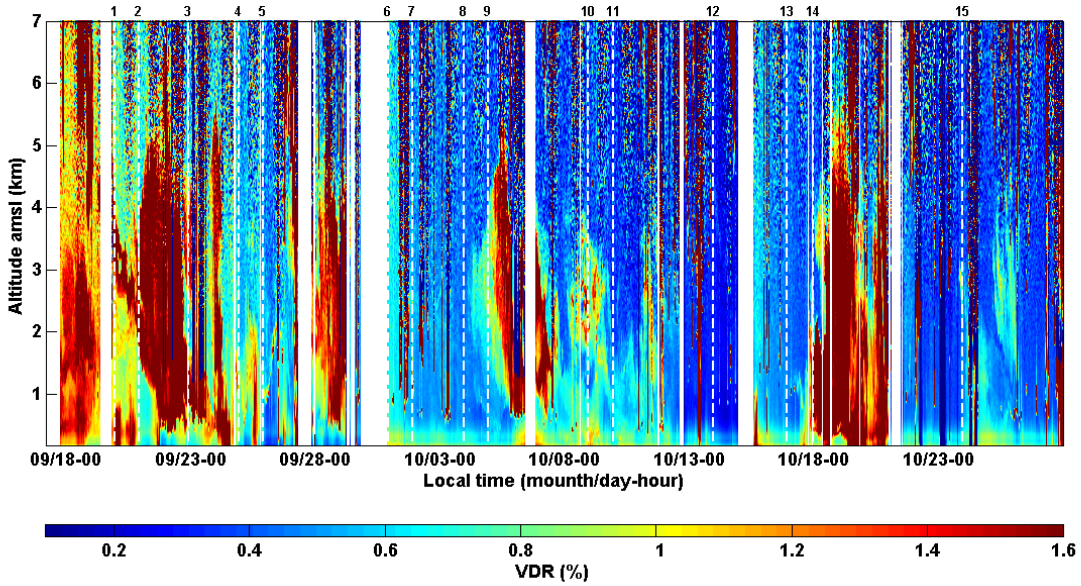

615

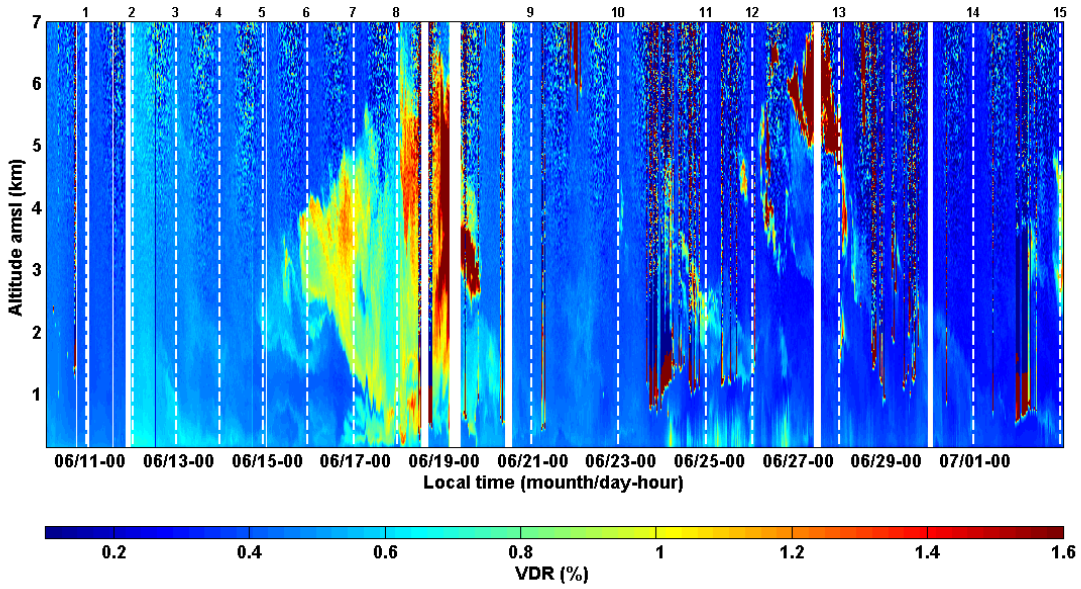

616

617 Figure 6: Volume Depolarization Ratio (VDR in %) evolution as a function of altitude (in km)
618 during HyMeX (up) and ChArMEx (down) experiments comparisons. The vertical white
619 dotted lines identify the coincidences with the CN at the top. The color bar ranges from low
620 VDR (blue) to high ones (red).

621

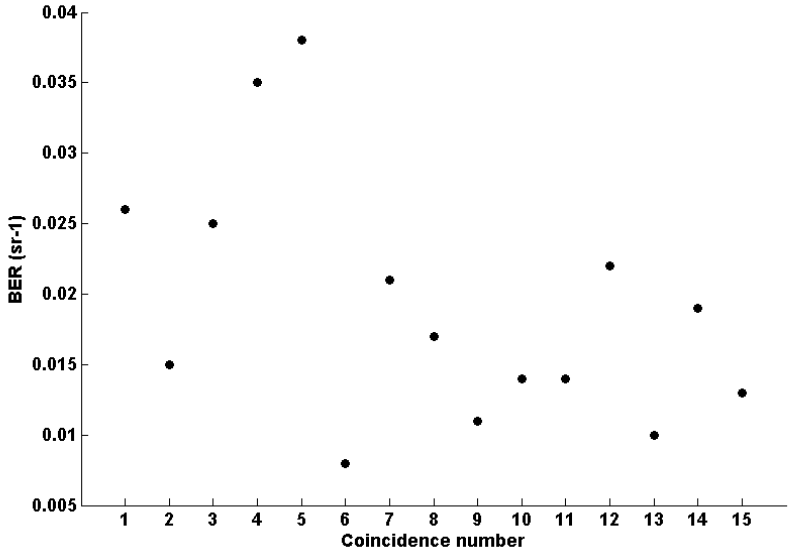

622

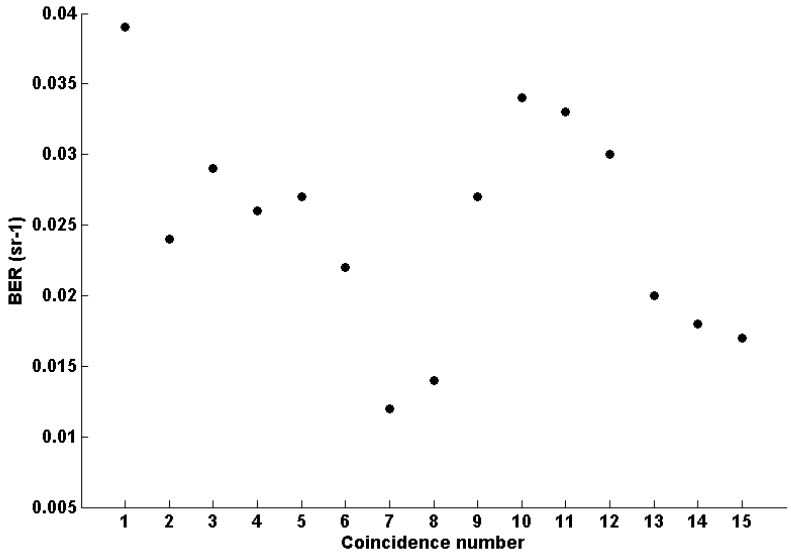

623

624 Figure 7: Column Backscatter to Extinction Ratio (BER in sr^{-1}) derived from WALI temporal
625 evolution for the different inter-comparisons exercises during HyMeX (up) and ChArMEx
626 (down) experiments. Abscisa represents the CN.

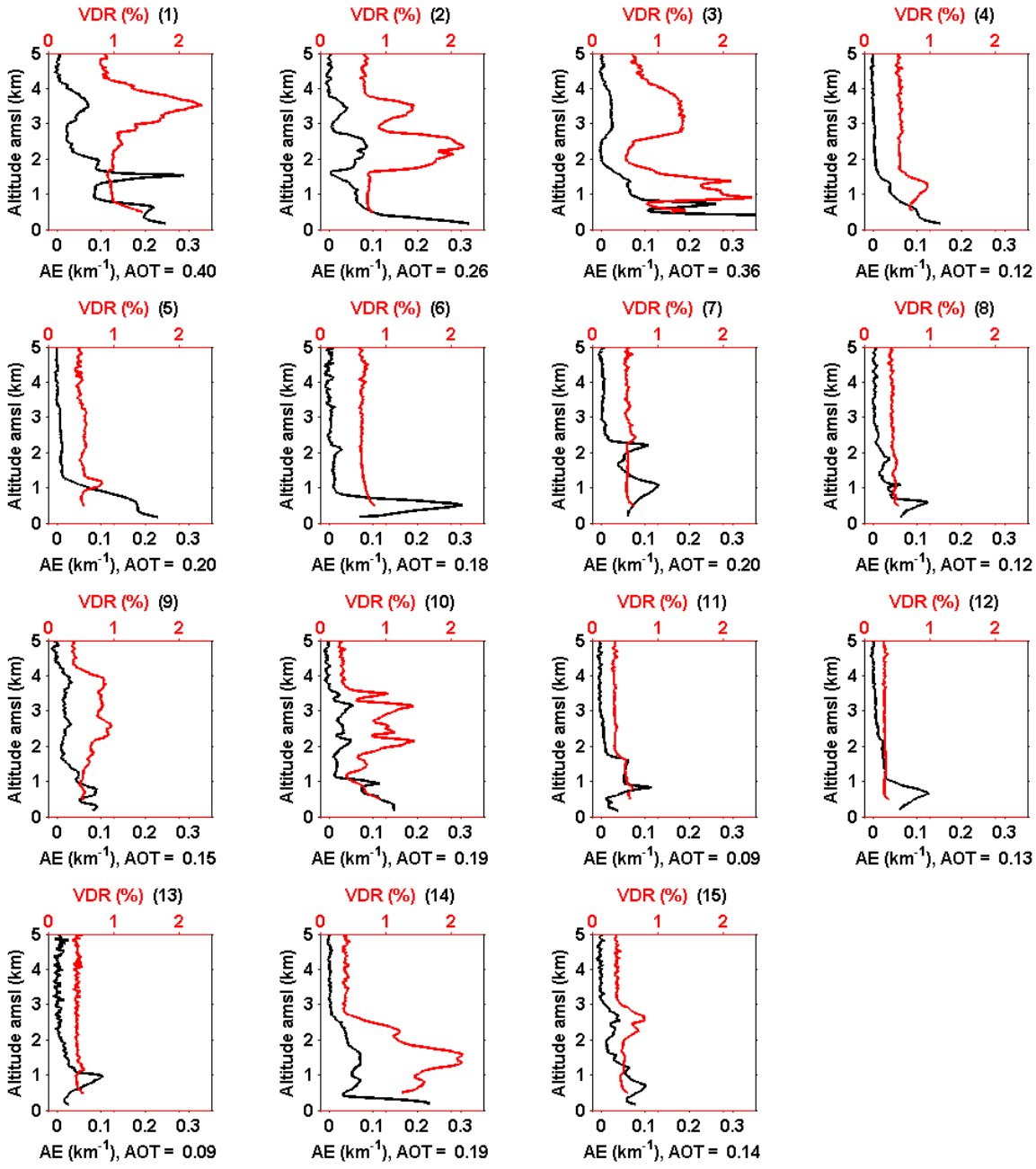

627

628 Figure 8: Aerosol extinction coefficient (AE in km^{-1}, black lines) and Volume Depolarization
629 Ratio (VDR in %, red lines) as a function of altitude for the inter-comparisons cases during
630 HyMeX experiment. For each individual case, the Atmospheric Optical Thickness (AOT) is
631 also reported. The CN is given in black at the top of each figure.

632

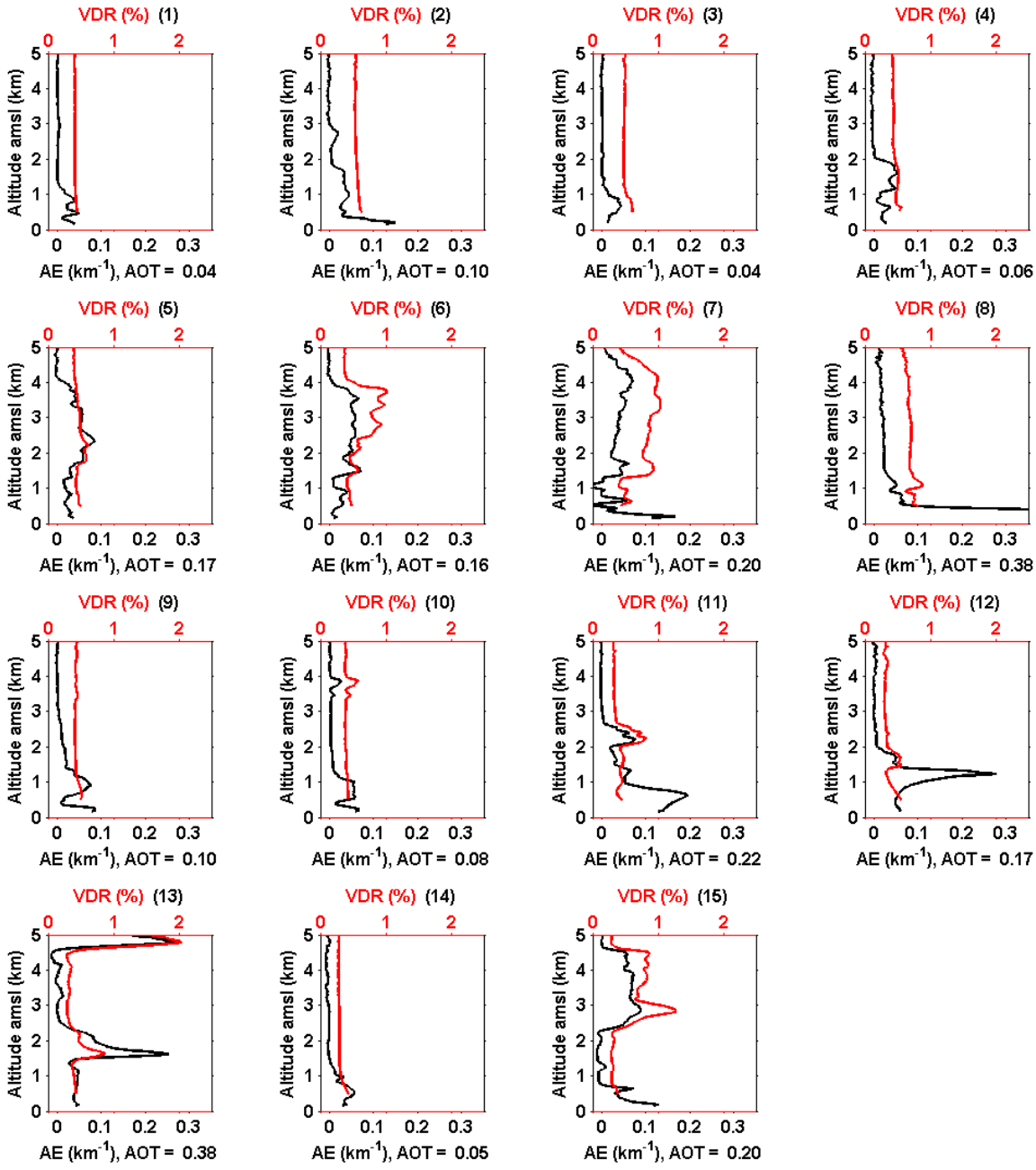

633

634 Figure 9: Same as Figure 8 for the ChArMEx experiment (June and July 2013).

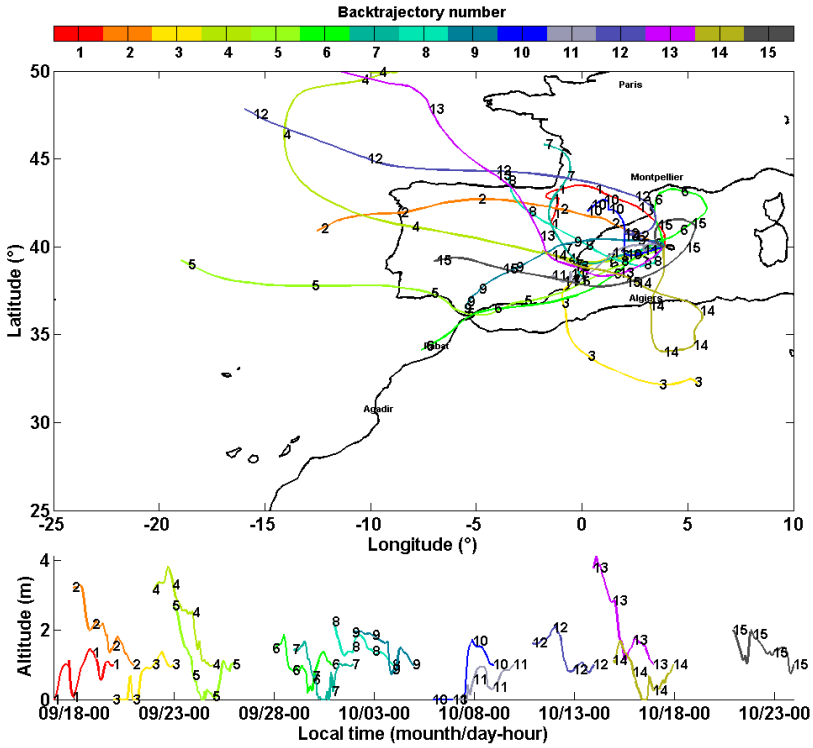

635

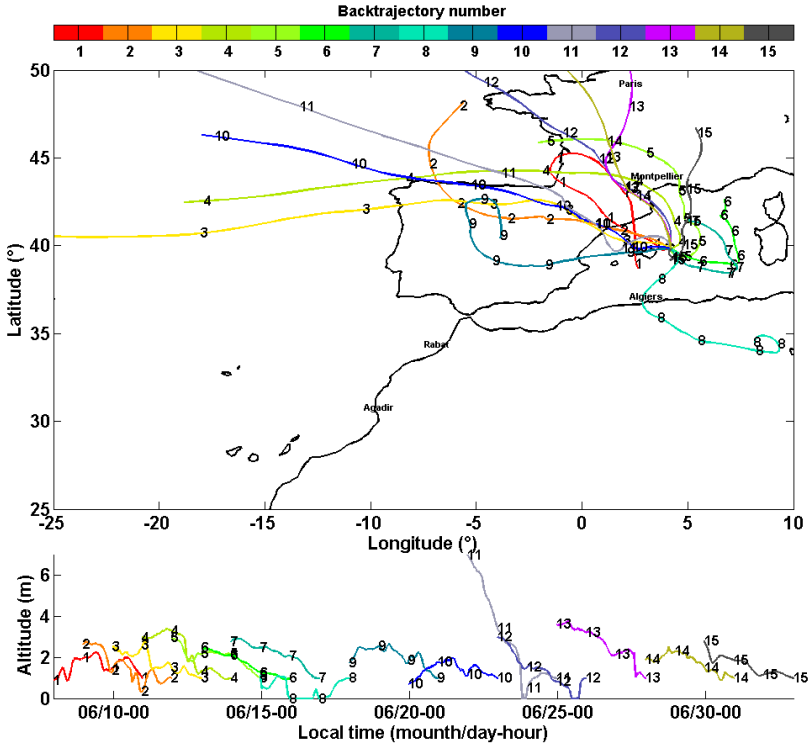

636

637 Figure 10: Back trajectories for each CN. They have been computed using the Hysplit model
638 (courtesy of NOAA Air Resources Laboratory; http://www.arl.noaa.gov). The end locations
639 of the air masses are for the sites of Ciutadella (up) and Mahon (down) for the HyMeX and
640 ChArMEx time periods, respectively, at the altitudes of 1 km amsl.

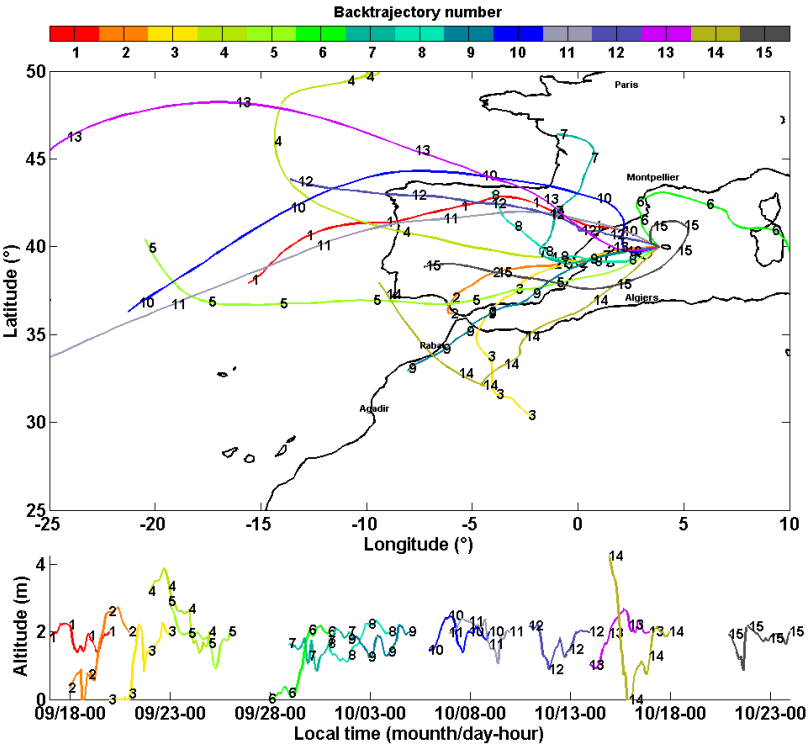

641

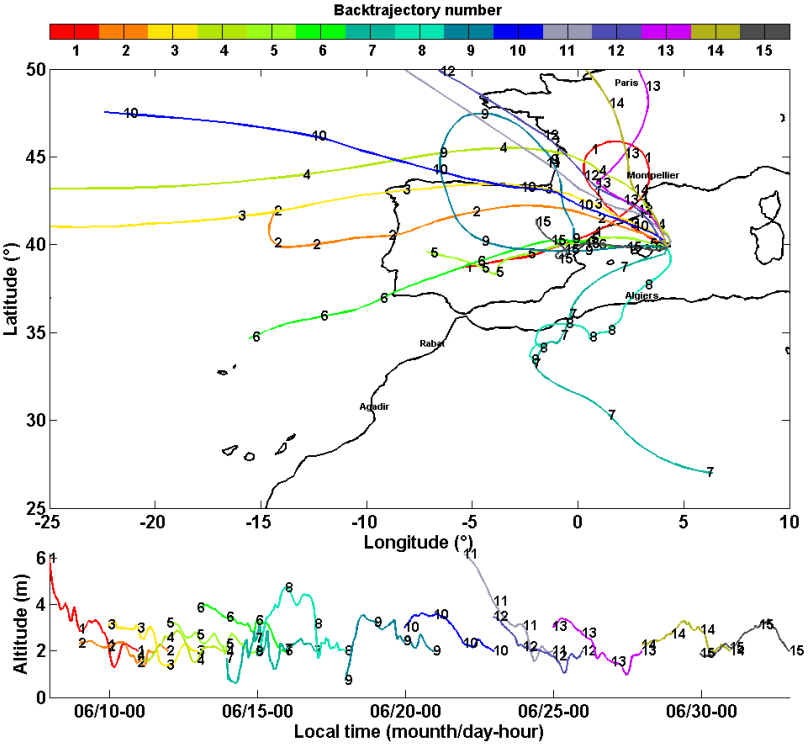

642

643 Figure 11: Same as Figure 10 for 2 km amsl.

644

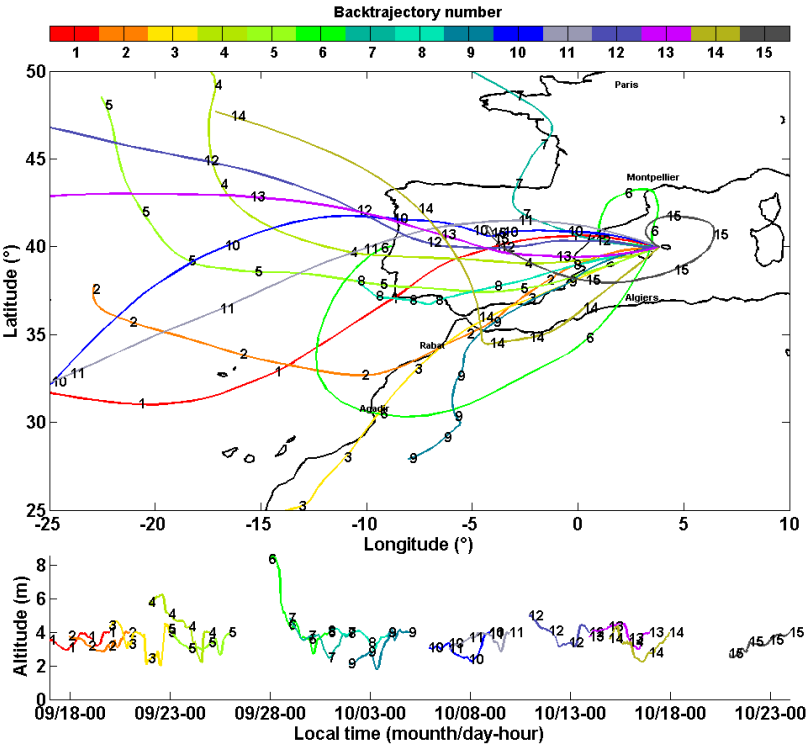

645

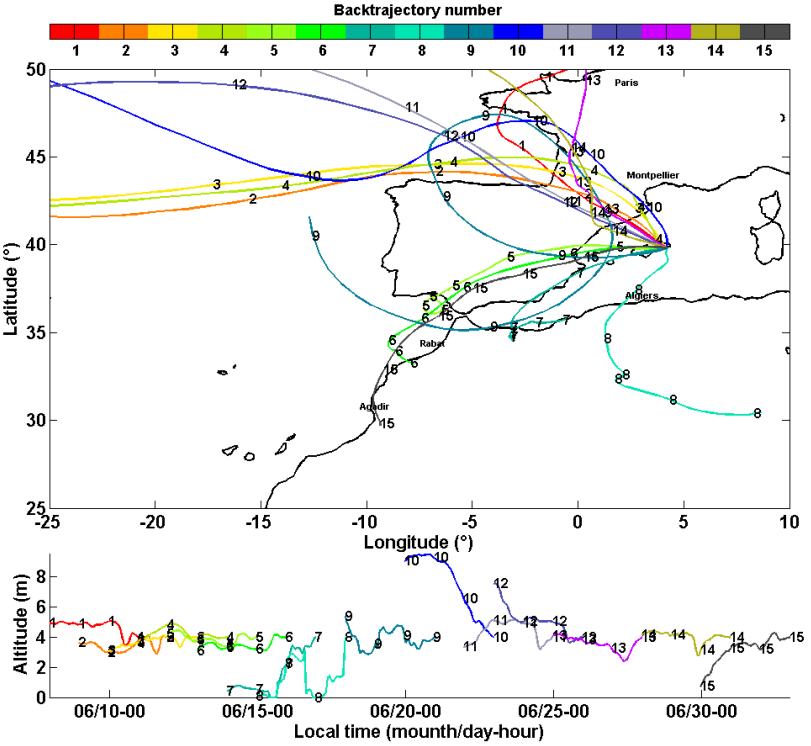

646

647 Figure 12: Same as Figure 10 for 4 km amsl.